Wavelength division multiplexing based on apodized planar holographic Bragg reflectors

Christoph M. Greiner, Dmitri Iazikov, and Thomas W. Mossberg

We report wavelength division multiplexing based on lithographically fabricated slab-waveguide-contained planar holographic Bragg reflectors (HBRs). Partial HBR diffractive contour writing and contour displacement are successfully demonstrated to enable precise bandpass engineering of multiplexer transfer functions and make possible compact-footprint devices based on hologram overlay. Four- and eight-channel multiplexers with channel spacings of ~50 and ~100 GHz, improved sidelobe suppression, and flattop passbands are demonstrated. When a second-order apodization effect, comprising effective waveguide refractive-index variation with written contour fraction, and the effect of hologram overlap on the hologram reflective amplitude are included in the simulation, excellent agreement between predicted and observed spectral passband profiles is obtained. With demonstrated simulation capability, the ability to fabricate general desired passband profiles becomes tractable.

OCIS codes: 060.1810, 060.4230, 090.4220.

1. Introduction

Planar holographic Bragg reflectors (HBRs)[1–4] are two-dimensional (2-D) lithographically scribed volume holograms contained within a slab waveguide. In the slab waveguide, optical signals propagate freely in two horizontal dimensions while being confined in the third vertical dimension—a geometry that allows 2-D Bragg structures to provide powerful spectral and spatial holographic functions within a fully integrated format. A single HBR can simultaneously spatially image an input signal to an output port (or from one point within an integrated photonic circuit to another) while at the same time providing spectral filtering of the signal. Unlike fiber and channel-waveguide gratings, where separation of the counterpropagating input and output signals typically requires additional elements, planar HBRs provide spatially distinct and thus easily accessed outputs.

HBRs constitute the building blocks of unique integrated photonic circuits that are based on the distributed nature of these devices. These distributed photonic circuits operate entirely without wire-analog channel waveguides and allow signal transport where signals freely overlap as they are imaged from active element. The distributed photonic circuit approach is more natural to the wave nature of light than the constraining wirelike channel waveguides typically used in integrated photonic circuits. Wire links are natural in electronics but are suboptimal for photonics. Our novel approach of integrated holographics combines the power of free-space optics and volume holography with a fully integrated environment.

The powerful volume-holographic function enabled by HBR structures provides, via computer-generated complex-shaped diffractive contours, fully optimized spatial mapping of an arbitrary complex input field wave front to an output field mode tailored to match the chosen output means. This broad in-plane spatial wave-front transformation capability contrasts with previously discussed 2-D distributed Bragg reflectors intended for out-of-plane applications such as laser feedback and outcoupling[5–7] and free-space to slab-waveguide beam coupling.[8,9] HBR spatial wave-front transformation, because of its holographic nature, is generally more powerful than that provided by simple conic section distributed Bragg reflectors,[10] whose focusing power degrades when input and output optics deviate from the point-source limit.

Recently we demonstrated[2] that photolithographic fabrication of HBRs in silica on silicon allows the highly accurate placement of constituent diffractive

The authors are with LightSmyth Technologies, Incorporated, 860 West Park Street, Suite 250, Eugene, Oregon 97041. The e-mail address for C. M. Greiner is cgreiner@lightsmyth.com.

Received 10 November 2003; revised manuscript received 6 May 2004; accepted 24 May 2004.

0003-6935/04/234575-09$15.00/0

contours as evidenced by fabrication of fully coherent centimeter-scale planar holographic structures. In addition, a robust and fabrication-friendly method to control the reflective amplitude of diffractive element contours by partial contour writing was presented.[4] Together, precise feature placement and partial contour writing provide control over the phase and amplitude of diffractive elements on an individual line basis. Such control is important for two reasons. Spectrally, it offers a pathway to unprecedented precision and flexibility in the design of HBR transfer functions through the tailoring of the diffractive element arrangement. Spatially, partial contour writing and displacement allow the overlay of several planar holograms on the same substrate—thus making it possible to design high-resolution (de)multiplexing devices for multiwavelength signals with a compact footprint. In this paper we demonstrate, for the first time to our knowledge, the application of these concepts to the spectral (bandpass) engineering of HBR-based multiplexing devices for dense wave-division multiplexing. We furthermore identify an important coupling between partial contour writing and the effective waveguide index that must be accounted for when amplitude apodization based on fractional contour writing is used.

2. Holographic Bragg Reflector Multiplexer Measurements and Simulations

A. Simple Unapodized Four-Channel 50-GHz Multiplexer

We begin the discussion of our results by introducing the general approach employed in our multiplexers and by reviewing some of the operational principles underlying the multiplexer-constituent HBRs. The interested reader is also referred to Refs. 1–4 for additional details on the HBR device physics.

Our approach to multiplexing based on HBRs is best explained with a specific device implementation. Although some of the details of this first device are specific to the multiplexer discussed here, the general approach is shared between all the devices presented in this paper unless specifically otherwise indicated.

The simple four-channel HBR multiplexer device of concern is shown in Fig. 1. It was fabricated to explore the general potential of the HBR approach for spectral multiplexing and to characterize basic device performance. The device top view of Fig. 1(a) illustrates the general multiplexer operational principle. An input signal is coupled into the planar device through an input (IN) channel waveguide from whose end point the input beam expands into a slab region. Shown to the right of the slab region are four stacked 5-mm-long holographic Bragg gratings whose vacuum resonance wavelengths, λ_1 through λ_4, increase with distance from the input port in increments of ~0.35 nm, corresponding to a multiplexer channel spacing of approximately 50 GHz. Note that the precise channel spacing and center wavelength values depend on the core thickness and refractive index of the specific waveguide in which the device design

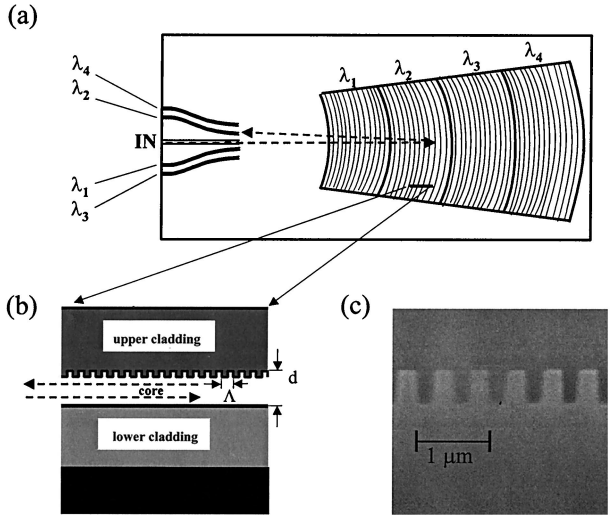

Fig. 1. Four-channel wavelength division multiplexer based on planar HBRs: (a) top view, (b) cross-sectional view, (c) cross-sectional scanning electron microscope photograph of the grating structure located at the upper core–cladding interface.

(comprising a periodic structure on a photomask) is lithographically realized.

The individual HBRs located to the right of the slab region spectrally filter the input signal and spatially direct light falling within their reflective resonance bandpass to one of the four wavelength-specific outputs. The multiplexer's wavelength-to-output port assignment follows the layout shown in Fig. 1(a). Consistent with our objective to first examine basic device operation and performance, no apodization was applied to the grating sections in this initial design. The HBR diffractive contours, represented in Fig. 1(a) by thin solid lines, can be designed individually to match the back-diffracted input field to the output port. For the devices described here, the diffractive contours were not optimized to provide maximal output coupling. In these early-stage devices, contours are configured as circular arcs concentric about the point midway between the end of the input channel waveguide and the beginning of the corresponding output channel waveguide. Fully optimized holographic contours will improve the input–output coupling by more effectively coupling to the mode of the output waveguide.

Figure 1(b) is a partial device cross section. The multiplexers discussed here are based on silica-on-silicon slab waveguides that consist of a central silica core with thickness $d = 2$ or 4 μm and bilateral 15-μm-thick cladding layers. For all the devices, the waveguide core exhibits a +0.8% index contrast with respect to its claddings. Also depicted at the upper core–cladding interface are cross sections of representative lithographically scribed grating diffractive contours. The diffractive contours, with a depth of ~450 nm, for all devices consist of trenches etched into the core and filled with cladding material. All gratings operate in first order with a contour spacing Λ of approximately 500 nm, i.e., one half of the in-

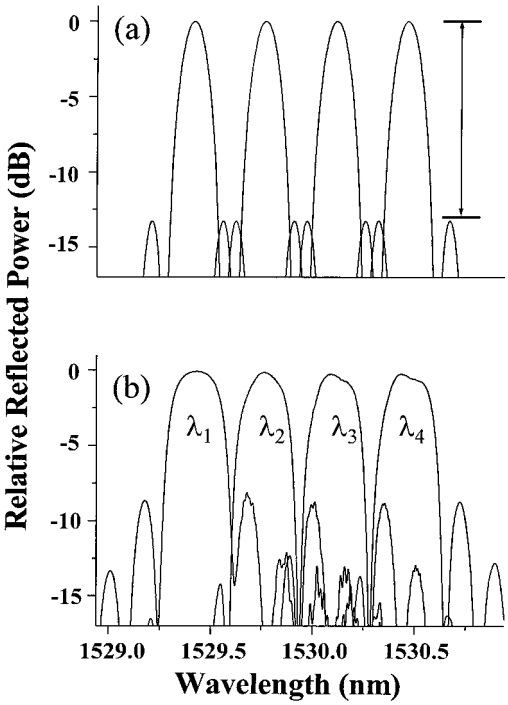

Fig. 2. Four-channel multiplexer spectral throughput: (a) simulated throughput, (b) measured response (for TE polarization). The arrows in (a) indicate the transform-limited sidelobe suppression provided by a uniform (unapodized) one-dimensional grating.

medium wavelength of resonant light. In the schematic cross section of Fig. 1(b) light enters the device from the left side and is coherently backscattered to the left by the collective action of the diffractive contours. Figure 1(c) is a cross-sectional scanning electron microscope photograph of the HBR grating structure located at the upper core–cladding interface.

The multiplexer's input–output channel-waveguide manifold [Fig. 1(a)] exhibits an interchannel spacing of 30 μm at the input side to the HBR slab region. Here, all waveguides have a design width of 12.7 μm, adiabatically increased from 6 μm at the die edge by a 0.5-mm-long taper. The output waveguides are angled with respect to the input waveguide. The angle of a given output waveguide is 0.1575°/(30 μm) × L, where L is the distance (in micrometers) between the end point of the input guide and the given output guide. The radius of the HBR's diffractive arc closest to the center of curvature is 3.5 mm. All devices discussed here occupy die areas of only approximately 1.7 cm^2 including access channel waveguides. All multiplexers reported on in this paper were fabricated from a laser-written reticle by use of a deep-ultraviolet optical stepper and standard etching, deposition, and annealing processes.

Figure 2(a) depicts the designed spectral transfer functions of the four multiplexer channels (bandpass profiles). We calculated these transfer functions using an extensive Fresnel–Huygens diffraction calculation in which the multiplexer structure was represented as a set of point scatterers that was derived from the spatial design data put on the photo mask. A Gaussian model input field with a $1/e$ diameter of 12 μm was employed. The transfer functions shown were calculated for the central points of the design output ports. Input field depletion was not taken into account in the simulation, so the validity of the calculation is restricted to devices of weak to moderate reflectivity. The relatively high adjacent sidelobes in the design spectral transfer functions are a direct consequence of the fact that this initial multiplexer design employs grating structures that are unapodized. The adjacent sidelobe suppression that can be seen in Fig. 2(a) is dictated by Fourier-transform theory (sinc function spectral response). For comparison, the transform-limited sidelobe suppression provided by a uniform grating is shown by the arrows on the right side of Fig. 2(a). In multiplexer designs discussed in the following sections, grating apodization is demonstrated to significantly improve sidelobe suppression. Figure 2(b) shows the measured spectral transfer functions of the four multiplexer output channels of the fabricated multiplexer for TE-polarized input light. The device was realized in a slab waveguide with $d = 4$ μm. To our knowledge the results shown comprise the first successful implementation of a photolithographically written HBR-based device for dense wave-division multiplexing and indicate an excellent coherent realization of the design structure. The average insertion loss, measured through coupled fibers, was found to be approximately 3 dB, which implies an HBR insertion loss of approximately 2 dB. Measured channel bandpass functions are broadened, and adjacent sidelobes are stronger than seen in the simulation—as expected at the achieved reflectivity levels. The longer wavelength channels (λ_2 through λ_4) are seen to exhibit passband shapes slightly different from the λ_1 channel. These are believed to arise from input depletion caused by signal travel through spatially preceding and partially resonant grating structures. Grating designs incorporating appropriate apodization acting to remove sidelobes of preceding gratings that are spectrally coincident with primary bandpasses of subsequent ones are expected to mitigate this effect.

B. Eight-Channel 100-GHz Multiplexer with Improved Sidelobe Suppression

An inherent advantage of the HBR technology is its capability to address multiplexing needs in a broad range of networks, including those based on hyperfine, dense, and coarse wavelength division multiplexing. Specifically, the approach provides for both the ability to implement almost arbitrary channel spacings (both uniform and nonuniform) as well as channel passbands that can be tailored to a high degree. To demonstrate these properties we fabricated an eight-channel HBR multiplexer with a channel spacing approximately twice that of the previous device (i.e., approximately 100 GHz) wherein channel transfer functions are designed to exhibit improved

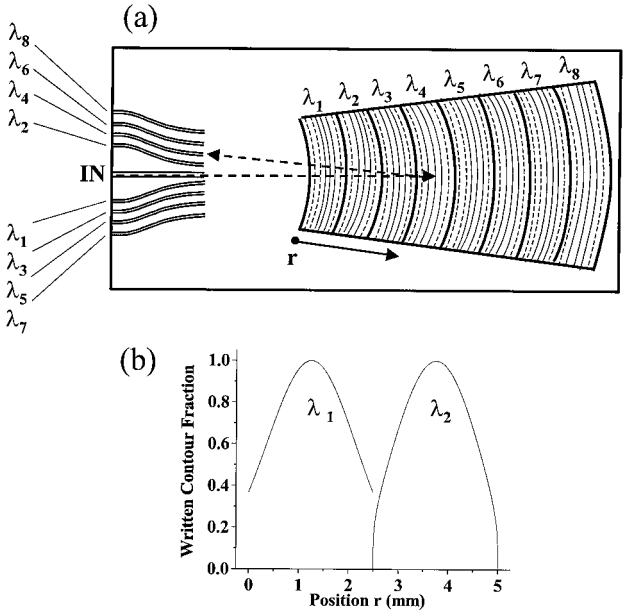

Fig. 3. (a) Schematic top view of an eight-channel HBR-based multiplexer, (b) apodization profiles for λ_1 and λ_2 multiplexer channels. All odd (even) channels have the same apodization as the λ_1 (λ_2) multiplexer channels.

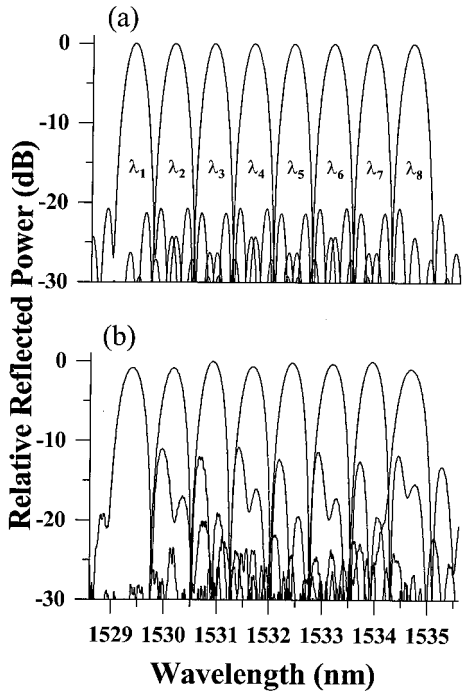

Fig. 4. Eight-channel multiplexer spectral throughput (core thickness $d = 4$ μm): (a) multiplexer design spectral transfer function, simulated with constant refractive index; (b) measured spectral response (for TE polarization).

adjacent sidelobe suppression compared with Fig. 2. The device layout is shown in Fig. 3(a). The multiplexer consists of eight stacked 2.5-mm-long apodized holographic Bragg gratings. Again, the individual channel gratings were spatially ordered so that their resonance wavelength increased with distance from the device input side. For the eight-channel multiplexer of Fig. 3(a), $d = 4$ μm. Engineering of the multiplexer's bandpass employs the fact that the grating spectral transfer function is determined by the detailed contour spacing and the relative reflective amplitude of the diffractive contours as a function of position along the input direction. Specifically, in the limit of weak device reflectivity, the device transfer function is proportional to the spatial Fourier transform of the complex amplitude relation coefficient as a function of device depth.[1] In the devices of concern here, diffractive contour amplitude and phase apodization is achieved by partial contour writing and positional displacements, respectively.[4] Two different amplitude-only apodization profiles, shown in Fig. 3(b), and based on the partial-fill method were employed in the device of Fig. 3(a). All gratings with an odd channel number are designed with the same apodization function as the one shown in Fig. 3(b) for the grating with center wavelength λ_1. All gratings with an even channel number are designed with the same apodization function as the one shown in Fig. 3(b) for the grating with center wavelength λ_2. Aside from the increased number of access channel waveguides, all parameters of the device access waveguide manifold shown in Fig. 3(a) are the same as for the device of Fig. 1(a).

Figure 4(a) depicts the designed spectral transfer function of the eight multiplexer channels. Note the improved suppression (>20 dB) of sidelobes immediately adjacent to the main channel passband compared with that evident in the designed bandpass of the unapodized four-channel device of Fig. 2(a). Figure 4(b) gives the measured spectral transfer function of the eight channels of the fabricated device for TE-polarized input light. Agreement between measured and designed performance is good except for the unexpectedly high sidelobes on the long-wavelength side of each primary passband. The device average intrinsic insertion loss (due to weak reflection) was found to be approximately 7 dB. The long-wavelength sidelobes in the measured multiplexer response are found to arise from a second-order apodization effect, detailed below, that was unaccounted for in the device designs. The second-order effect comprises an effective refractive-index variation inadvertently introduced by use of partial contour fill to effect amplitude apodization. Note that the spectral transfer functions of the channels to the left (λ_1) and right (λ_8) in Fig. 4(b) can be seen to exhibit slightly higher insertion losses and broader bandpasses than all other channels of the same respective apodization function. This effect was caused by a photolithographic fabrication error wherein gratings located at the outer edges of the field of the deep-ultraviolet stepper were only partially written. Specifically, the lengths of the first and last gratings (with respect to the input port), corresponding to center wavelengths λ_1 and λ_8, were reduced by 10% and 20%, respectively.

In the present multiplexer design, apodization of

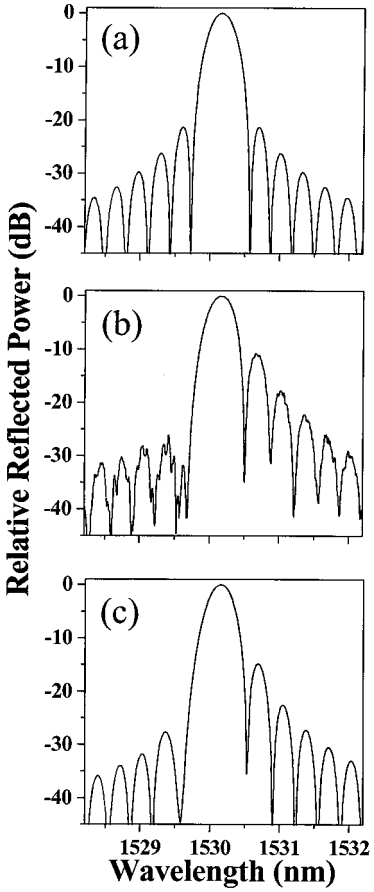

Fig. 5. Detail of the passband function for the second multiplexer channel (λ_2): (a) simulated throughput, calculated with constant effective index; (b) measured throughput (for TE polarization); (c) simulated throughput, calculated for apodization-induced effective index changes.

the reflective amplitude of HBR diffractive contours is achieved through partial contour writing.[4] Nominally continuous diffractive contours are written fractionally, with the written contour fraction determining the contour's reflective amplitude. Contour writing occurs through etching (and filling with cladding material) of trenches into the core. Variations in the written trench fraction due to amplitude apodization lead to differences in waveguide morphology that cause variations in the slab-waveguide effective refractive index and consequently the Bragg resonance condition. Measurements performed on various test grating structures, each having diffractive contours of a fixed written fraction, show a small and approximately linear variation of effective waveguide refractive index with the written trench fraction. Specifically, for a slab-waveguide core of thickness of $d = 4$ μm and 450-nm-deep diffractive trenches, the effective waveguide index was measured to vary as

$$n_{\text{eff}}(r) = n_0[1 - 2 \times 10^{-4} G(r)],$$

where n_0 is the effective index of the slab waveguide in the absence of the HBR contours and $G(r)$ is the written diffractive contour fraction at position r.

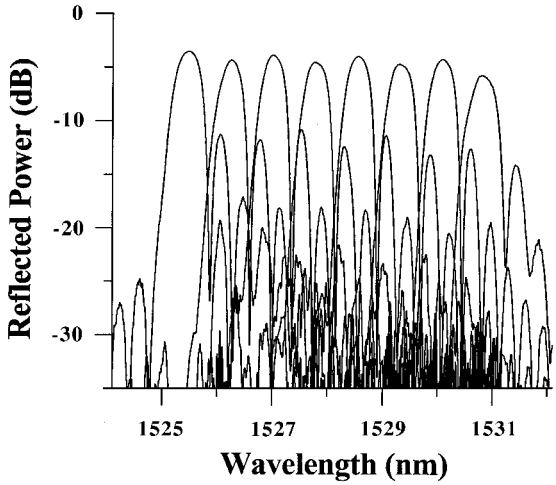

Fig. 6. Spectral throughput of an eight-channel multiplexer (core thickness $d = 2$ μm).

In Figure 5 we explore the effect of the apodization-induced resonance shifts on the multiplexer spectral transfer function. Figure 5(a) is a blowup of the original design passband function for the second multiplexer channel (λ_2) calculated with constant effective slab-waveguide refractive index. Figure 5(b) shows the detailed measured spectral response for the same channel. Figure 5(c) shows the passband profile simulated including the effect of the measured apodization-induced effective refractive-index changes. A comparison of Figs. 5(b) and 5(c) shows that the simulation now clearly reproduces all features of the fabricated device. The value of n_0 was chosen so that the center wavelengths of the simulated and measured device responses, Figs. 5(c) and 5(b), respectively, coincide. To obtain Fig. 5(a), $G(r)$ was set to unity and the resulting spectrum was shifted by −70 pm. Again, this was done so that the center wavelengths of Figs. 5(a) and 5(b) coincided to facilitate comparison.

The measured multiplexer insertion losses of Fig. 4 arise primarily from low overall reflectivity rather than true loss from scattering or other means. In reflective devices such as the ones considered here, the overall achievable reflectivity depends on the diffractive element index contrast, the total available device length, and the overlap of the diffractive elements (contours) with the given mode field distribution. For fixed index contrast, device length, and diffractive contour depth, the overall device reflectivity can be improved by a decrease (up to a certain limit) in the core diameter that in turn enhances the mode field-grating overlap. This approach is demonstrated in Fig. 6, where the multiplexer design structure of Fig. 4 was implemented in a silica-on-silicon slab waveguide with a core thickness of $d = 2$ μm. The graph shows the measured (TE-polarized) spectral response for the eight multiplexer channels. The fiber-coupled average insertion loss is approximately 4 dB, which implies a device intrinsic loss of 3 dB and an improvement of overall reflectivity by 4 dB

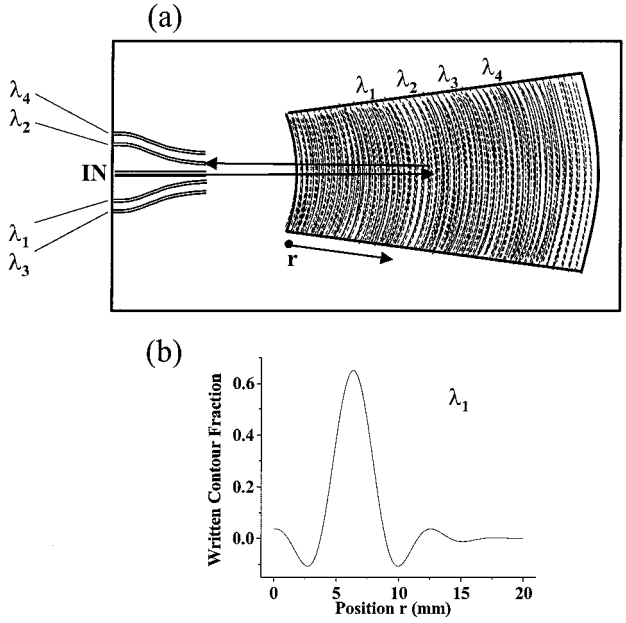

Fig. 7. (a) Schematic top view of a four-channel flattop HBR-based multiplexer based on overlaid planar holograms, (b) apodization profile for the leftmost (λ_1) multiplexer channel.

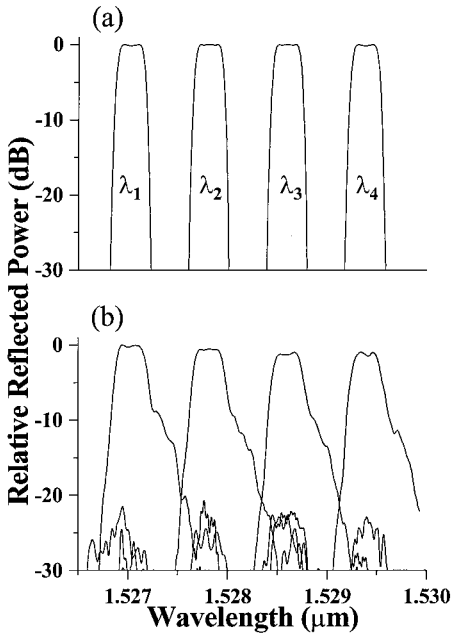

Fig. 8. (a) Multiplexer spectral transfer function simulated with constant effective index, (b) measured multiplexer spectral transfer function (for TE polarization).

compared with Fig. 4. Note that the measured bandpass profiles of Fig. 6 are slightly broader than the weak reflection limit simulation of Fig. 4, consistent with the measured 50% reflectivity. Note also that the multiplexer of Fig. 6 was fabricated with the same reticle as the device of Fig. 4(b), resulting in a similar defect of the rightmost (λ_8) channel grating and a consequently higher than average insertion loss.

C. Four-Channel 100-GHz Multiplexer Based on Overlaid Apodized Holographic Bragg Reflectors

Lithographically enabled partial writing (amplitude apodization) and displacement (phase shifts) of contours not only make possible the precise bandpass engineering of multiplexer spectral transfer functions but also enables the overlay of planar holograms[1] on the same substrate providing for compact footprint devices. We apply this concept to the design of a four-channel, ~100-GHz channel spacing, HBR-based multiplexer with designed flattop channel passbands. Figure 7(a) is a top-view schematic of the overlain HBR devices. The device comprises apodized individual-channel HBRs that are staggered along the input beam direction but are heavily overlapping as well. Each hologram is realized with a maximum written trench fraction of 0.65 that ensures that the aggregate (summed over all holograms) written trench fraction at any given position in the multiplexer does not exceed unity significantly (<1.1). The multiplexer is based on a 2-μm-thick slab waveguide. Parameters of the input–output waveguide manifold are the same as for the device of Fig. 1. Figure 7(b) depicts the apodization profile of the λ_1 channel. Negative portions in the apodization function correspond to π phase shifts and were realized by means of spatially offsetting the diffractive contours of the corresponding grating sections by $\lambda/4$ (in-guide wavelength) spatial shifts with respect to the positive grating sections.

Figures 8(a) and 8(b) depict the simulated and measured spectral transfer functions of the various multiplexer channels for TE-polarized input light, respectively. The measured passbands clearly show the designed flat passband and channel spacing. The multiplexer's adjacent channel isolation exceeds −22 dB. This is excellent for a first iteration design. The absolute multiplexer insertion loss through coupled fibers was approximately 6 dB, implying a 5-dB device intrinsic loss, primarily caused by low device reflection. Discrepancies between measured and designed channel transfer functions such as the long-wavelength shoulder of the measurement arise principally from two factors. First, apodization-induced effective index changes are not compensated for in the present multiplexer design. Second, in designing the device, we overlaid the various individual-channel HBRs without taking detailed precaution to avoid overlap of diffractive contours belonging to different holograms. Because of the present constant-etch-depth multiplexer layout, the overall device reflective strength at a given position is not a linear sum of all contributing diffractive contours at that location. Rather, portions of a given hologram that coincide with diffractive contours of a different grating exhibit a reflective amplitude that is reduced from its design value. Consequently, the actual apodization of a planar hologram is altered from the original design value through two position-dependent effects, i.e., (1) variations in slab-waveguide effective refractive index and

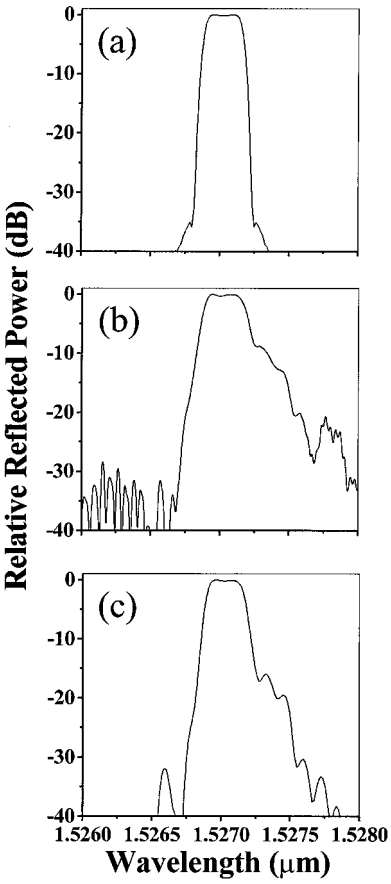

Fig. 9. Blowup of the leftmost multiplexer channel: (a) constant effective index simulation, (b) measured passband, (c) multiplexer throughput calculated including apodization-induced effective index variations and reflective amplitude reduction due to hologram overlay.

(2) variations in expected reflective amplitude. Both effects must be accounted for to correctly predict the bandpass function of the fabricated multiplexers. Consideration of these same effects at the design stage allows for precisely crafted bandpass engineering.

Figure 9 explores the effect of the above-described phenomena on the spectral transfer function of the λ_1 multiplexer channel. Figure 9(a) is a blowup of the original design passband function calculated with constant effective index and without account for the reduction of the reflective amplitude caused by hologram overlap. Figure 9(b) shows the detailed measured TE-polarized spectral response for the same channel. Figure 9(c) shows the passband profile simulated with both the spatially varying effective refractive index and the reflective amplitude changes accounted for as described below.

The apodization and overlap effects lead to a position-dependent effective waveguide refractive index that we model (guided by test results on auxiliary structures) as

$$n_{\text{eff}}(r) = n_0\{1 - 6 \times 10^{-4}[1 - R(r)]\},$$

where $R(r)$ is the unetched (no written trenches) fraction of a slab waveguide at each position r within the device and n_0 is the effective index of the slab waveguide in the absence the HBR contours. $R(r)$ was calculated according to

$$R(r) = \prod_{i=1}^{N} [1 - \alpha_i G_i(r)],$$

where $G_i(r)$ is the written diffractive contour fraction of the ith planar grating at position r and α_i is its duty cycle. The summation runs over all HBRs written. In the present multiplexer design all gratings operate in the first grating order, thus $\alpha_i = 0.5$ for $i = 1, \ldots, N$.

The reflective amplitude of the jth planar hologram as modified by grating superimposition is written as

$$A_j(r) = A_j'(r) \prod_{i=1, i\neq j}^{N} [1 - \alpha_i G_i(r)],$$

where $A_j'(r)$ is the apodization function that pertains in the absence of overlap. The sum runs over all HBRs except for the jth hologram. A comparison of Figs. 9(b) and 9(c) shows that the simulation now clearly reproduces all features of the fabricated device. The simulated passbands shown in Fig. 9 were adjusted to exhibit coincident center wavelengths to facilitate a straightforward profile comparison. Overall, the results shown in Figs. 8 and 9 demonstrate both the feasibility of spectral passband engineering and the ability to construct devices based on overlaid HBRs.

The agreement between the simulation of Fig. 9(c) and the measured bandpass spectrum of Fig. 9(b) is quite excellent. It is apparent from this agreement that the photolithographic fabrication method employed reproduced the design set of grating elements with great precision. The multiplexers studied here were designed without consideration of the effective refractive-index variation with amplitude apodization and the effect of hologram overlay on reflective amplitude. Multiplexer designs can be simply corrected for the effect of apodization-induced effective refractive-index changes by means of scaling the separation between grating lines to keep optical path distances constant. Overlay-induced reflective amplitude reduction can be avoided by use of higher grating orders or lower peak fill fractions and by implementation of a design algorithm wherein spatially overlapping contour elements are displaced to avoid overlap. Alternatively, overlap effects can simply be added to the design algorithm. It should be noted that HBR overlap multiplicity is constrained by the required reflective strength. For a fixed diffractive contour index contrast and waveguide dimensional parameters, the net reflective strength per unit surface area is subject to constraints. Evaluation of the details of these constraints is beyond the scope of this study, but it appears that overlay has advantages over spatial stacking when, for example, spectral resolution necessitates structures that extend

spatially beyond the device length required to obtain adequate reflectivity. In this case, overlay of spatially extended but locally weakly reflecting (low-partial-fill) structures can provide a pathway to high-resolution multiplexers in dimensions smaller than those necessary in the case of spatially separated HBR structures.

D. Polarization-Dependent Properties

The measurements shown in this study employ TE-polarized input signals. For TM input polarization, the grating bandpass functions were observed to shift by approximately +0.65 nm (+0.72 nm) for devices with a core thickness of $d = 2$ μm ($d = 4$ μm). Measurements of other HBR devices have indicated that polarization-dependent wavelength shifts originate from residual slab waveguide birefringence.[3] We note that sampling of HBR structures by channel waveguides[3] offers a pathway to mitigate the observed polarization-dependent wavelength shifts and is projected to yield a device fully compliant with today's standards for dense wavelength division multiplexing. Alternatively, we found that certain proprietary internal waveguide design modifications virtually eliminate polarization-related bandpass shifts.

No polarization-dependent loss (PDL) was measured for multiplexers implemented in the $d =$ 4-μm-thick slab waveguides, whereas approximately 0.3 dB of PDL was observed with $d = 2$ μm. For $d = 2$ μm, the observed PDL is consistent with magnitudes expected to arise from access channel waveguides, either through propagation loss or fiber-to-waveguide coupling. This was corroborated by independent measurement of the latter. In the limit of strong grating reflectivity, the reflective bandwidth ratio for TE and TM polarization, γ, is directly proportional to that of the TE and TM amplitude reflection coefficients and can be used to estimate the latter. From test results for $d = 2$, we find $\gamma = 1.018$. On the basis of this value we estimate the weak-reflectivity ($R \approx 10\%$) PDL inherent to the HBR to be approximately 0.15 dB and correspondingly less for more strongly reflecting devices as is the case with the muliplexers reported here.

3. Conclusions

As constructed, the present HBR-based multiplexers operate at low to moderate reflectivity. Detailed calculations, presented elsewhere,[11] indicate that achievable alterations in diffractive structure geometry and refractive-index contrast will lead to HBRs of centimeter scale having strong reflectivity and thus low insertion loss over an aggregate bandwidth as large as several hundred nanometers, i.e., broad enough, for example, to support a 16-channel coarse wavelength division multiplexer with 13-nm-wide flattop passbands. An added benefit of the coarse wavelength division multiplexing application is that the polarization-dependent wavelength shifts observed in the present study are essentially immaterial because they represent only a small fraction of the device passband.

Furthermore, a wide range of alternative HBR internal designs is possible providing even broader aggregate reflection bands while being fully consistent with low loss at the fiber-to-die interface. With these designs it appears entirely feasible to integrate much of the functionality currently attributed to discrete-component-based thin-film filters into the fully integrated environment.

4. Summary

In summary, we have demonstrated the viability of planar HBRs as powerful building blocks for wavelength division multiplexers. Our present results demonstrate, for the first time to our knowledge, (1) the application of the simultaneous spectral and spatial processing capability of photolithographically written HBR structures to dense wavelength division multiplexing, (2) the successful bandpass engineering of HBR-based multiplexers by fractional writing and positional displacements of constituent diffractive contours, and (3) the spatial overlay of multiple HBR structures to create high-resolution multiport integrated photonic devices of compact footprint. More generally, the powerful spectral and spatial beam control inherent to the integrated holographics approach offers the possibility of channel-waveguide-free integrated photonic circuits, termed distributed photonic circuits, wherein signal routing and processing occurs entirely through interaction with distributed diffractive structures like the HBR. Furthermore, as planar surface-relief structures, HBRs promise consistency with low-cost, mass-production, nanoreplication techniques such as hot embossing or nanoimprint lithography. In embossed or stamped formats, HBRs present an economic route to volume production of high-performance optical communications components for data communications and to access networks.

References

1. T. W. Mossberg, "Planar holographic optical processing devices," Opt. Lett. **26,** 414–416 (2001).
2. C. Greiner, D. Iazikov, and T. W. Mossberg, "Fourier-transform-limited performance of a lithographically-scribed planar holographic Bragg reflector," Photon. Technol. Lett. **16,** 840–842 (2004).
3. C. Greiner, D. Iazikov, and T. W. Mossberg, "Lithgraphically-fabricated planar holographic Bragg reflectors," J. Lightwave Technol. **22,** 136–145 (2004).
4. D. Iazikov, C. Greiner, and T. W. Mossberg, "Effective gray scale in lithographically scribed planar holographic Bragg reflectors," Appl. Opt. **43,** 1149–1155 (2004).
5. T. Erdogan and D. G. Hall, "Circularly symmetric distributed feedback laser: coupled mode treatment of TE vector fields," IEEE J. Quantum Electron. **28,** 612–623 (1992).
6. R. H. Jordan, D. G. Hall, O. King, G. Wicks, and S. Rishton, "Lasing behavior of circular grating surface-emitting semiconductor lasers," J. Opt. Soc. Am. B **14,** 449–453 (1997).
7. S. Kristjansson, N. Eriksson, A. Larsson, R. S. Penner, and M. Fallahi, "Observation of stable cylindrical modes in electrically pumped circular grating-coupled surface-emitting lasers," Appl. Opt. **39,** 1946–1953 (2000).
8. M. Li, B. S. Luo, C. P. Grover, Y. Feng, and H. C. Liu, "Waveguide grating coupler with a tailored spectral response

based on a computer-generated waveguide hologram," Opt. Lett. **24,** 655–657 (1999).
9. J. Backlund, J. Bengtsson, C. Carlstrom, and A. Larsson, "Input waveguide grating couplers designed for a desired wavelength and polarization response," Appl. Opt. **41,** 2818–2825 (2002).
10. C. H. Henry, R. F. Kazarinov, Y. Shani, R. C. Kistler, V. Pol, and K. J. Orlowsky, "Four-channel wavelength division multiplexers and bandpass filters based on elliptical Bragg reflectors," J. Lightwave Technol. **8,** 748–755 (1990).
11. D. Iazikov, C. Greiner, and T. W. Mossberg, "Apodizable integrated filters for coarse WDM and FTTH-type applications," J. Lightwave Technol. **22,** 1402–1407 (2004).